

A Correlated Search for Local Dwarf Galaxies in GALFA-HI and Pan-STARRS

DANIEL DEFELIPPIS,¹ MARY PUTMAN,¹ AND ERIK TOLLERUD²

¹*Department of Astronomy, Columbia University, 550 West 120th Street, New York, NY 10027, USA*

²*Space Telescope Science Institute, 3700 San Martin Drive, Baltimore, MD 21218, USA*

ABSTRACT

In recent years, ultrafaint dwarf (UFD) galaxies have been found through systematic searches of large optical surveys. However, the existence of Leo T, a nearby gas-rich dwarf, suggests that there could be other nearby UFDs that are optically obscured but have gas detectable at nonoptical wavelengths. With this in mind, we perform a search of the full Galactic Arecibo *L*-band Feed Array HI (GALFA-HI) survey, a radio survey which covers one-third of the sky at velocities $-650 < V_{LSR} < +650$ km s⁻¹, for neutral hydrogen sources. We are able to probe regions of the sky at lower Galactic latitudes and smaller $|V_{LSR}|$ compared to previous explorations. We use the Source Finding Application (SoFiA) on GALFA-HI and select all sources with similar properties to Leo T and other local dwarf galaxies. We find 690 dwarf galaxy candidates, one of which is particularly promising and likely a new galaxy near the Galactic plane ($b = -8^\circ$) that is comparable in velocity width and HI-flux to other recently discovered local volume galaxies. We find we are sensitive to Leo T-like objects out to 1 Mpc at velocities clear from background HI emission. We check each candidate’s corresponding optical fields from Pan-STARRS and fit stars drawn from isochrones, but find no evidence of stellar populations. We thus find no other Leo T-like dwarfs within 500 kpc of the Milky Way in the one-third of the sky covered by the GALFA-HI footprint and discuss our nondetection in a cosmological context.

Keywords: galaxies: dwarf — Local Group — radio lines: ISM — surveys

1. INTRODUCTION

The Milky Way (MW) environment provides a unique opportunity to study galaxy formation and evolution with its observed dwarf galaxy population. The smallest dwarf galaxies are the dimmest, and also the most abundant type of galaxy in the local environment. There have been numerous searches for, and discoveries of, individual ultrafaint dwarfs (UFDs) in the past decade (e.g., Willman et al. 2005; Belokurov et al. 2006; Zucker et al. 2006; Belokurov et al. 2007; Irwin et al. 2007). More recently, systematic searches of large optical surveys such as the Sloan Digital Sky Survey (SDSS; Walsh et al. 2009) and the Dark Energy Survey (Bechtol et al. 2015), as well as radio surveys such as the Galactic Arecibo *L*-band Feed Array (GALFA) Survey (Saul et al. 2012) and Arecibo Legacy Fast ALFA (ALFALFA) Survey (Adams et al. 2013) have yielded even more UFD candidates.

Discoveries of local dwarfs have gone a long way in addressing conflicts between the MW’s environment and cosmological simulations. For instance, the discrepancy between the number of MW satellites found observationally and in simulations first identified by Klypin et al. (1999) – the so-called “missing satellites problem” – has been significantly reduced by simply detecting more dwarfs (Simon & Geha 2007). Recent simulations have found satellite populations consistent with current observations (Garrison-Kimmel

et al. 2019), but discrepancies between the observed MW environment and simulated environments still remain, especially in the local volume (Klypin et al. 2015). Based on SDSS data there are potentially hundreds of faint satellites that could be revealed by deeper surveys (Tollerud et al. 2008; Hargis et al. 2014). Though folding in data from the Dark Energy Survey lowers that estimate considerably (Newton et al. 2018), there may still be ~ 100 undiscovered satellites that are “missing” simply due to the incompleteness of large sky surveys, a conclusion also supported by Fritz et al. (2018)’s finding that there should be a population of undiscovered UFDs at the apocenter, thus illustrating the importance of looking for dwarfs in previously unsearched regions of the sky.

Many such unsearched regions remain that way due to various observational difficulties. Areas covered by the Galactic plane are essentially opaque in optical wavelengths, and in velocity space, Galactic emission dominates at low velocities and complicates spectral follow-up at all wavelengths. Thus far, searches for dwarf galaxies have focused on observing their stellar light at high Galactic latitude, thus limiting the area surveyed both spatially and in distance, and biasing surveys toward those galaxies with significant stellar populations.

Though first detected optically, a UFD called Leo T has been found to have recent star formation from < 1 Gyr ago and a sizable reservoir of neutral hydrogen gas (HI) (Irwin et al. 2007; Weisz et al. 2014). Why Leo T even exists is still not clear, as most reionization models strip dwarfs of this mass of their gas and prevent them from accreting gas after $z = 1$ which would be necessary for recent star formation (e.g. Ricotti & Gnedin 2005; Ricotti et al. 2016). However, some models predict dwarfs could exist as gas-rich Leo T-like objects if they evolved in relative isolation from the MW (Ricotti 2009). Such models thus imply there are dwarfs that can be detected by observing their gas rather than their stars, which would allow previously unobservable areas of the sky to be probed. If such dwarfs exist and have properties similar to Leo T ($M_{\text{HI}} \sim 4.1 \times 10^5 M_{\odot}$ and $w_{50} \sim 17 \text{ km s}^{-1}$ from Adams & Oosterloo 2018), they should be detectable with high resolution and sensitivity by HI surveys within and beyond the Local Group.

With this motivation in mind, this paper attempts to find and catalog new dwarf galaxy candidates from the full GALFA-HI survey, an HI survey that covers $\approx 1/3$ of the sky at unprecedented spatial and velocity resolution (Peek et al. 2018). We subsequently correlate the candidates with the optical Pan-STARRS survey to investigate if they have a detectable stellar population. In Section 2 we describe the surveys and software used, and detail our analysis methodologies. In Section 3 we present a catalog of dwarf galaxy candidates from our analysis, which includes a very strong candidate galaxy in the Galactic plane, and in Section 4 we compare our catalog to other surveys of HI objects. Finally, we discuss the implications of our nondetections in Section 5, and summarize our results in Section 6.

2. METHODS

2.1. Surveys

The Galactic Arecibo L -band Feed Array HI (GALFA-HI) survey is a high spatial (4 arcmin) and spectral (0.74 km s^{-1} , smoothed) resolution survey of HI in the MW environment. It comprises 225 data cubes with $1'$ pixels that cover declinations between -1° and 38° across all right ascensions, and covers velocities from $-650 < V_{\text{LSR}} < +650 \text{ km s}^{-1}$. The survey includes a wide range of Galactic latitudes and passes through the plane of the MW twice. We utilize GALFA-HI DR2 (Peek et al. 2018) for this study as it covers the complete 32% of the sky with relatively uniform coverage. Peek et al. (2018) quote a median root mean square (rms) noise of 0.15 K (16 mJy per beam), in a 1 km s^{-1} channel for DR2. We note that GALFA-HI DR1 (Peek et al. 2011) is deeper in some areas, but only covers approximately half the sky area in a nonuniform way. See Saul et al. (2012) for a compact cloud catalog using the DR1 data and Donovan Meyer et al.

(2015) for an investigation of UV counterparts to these HI candidates.

To correlate objects found in GALFA-HI with optical observations, we require an optical survey with an overlapping footprint. The Pan-STARRS survey fits this need, as it covers all parts of the sky north of -30° decl. and thus fully contains the area covered by GALFA-HI. Pan-STARRS was run using the 1.8 m telescope at the University of Hawaii that mapped the sky in five optical and infrared bands: $g, r, i, z,$ and y . For further details, see Chambers et al. (2016).

2.2. HI Source Finding

We used the Source Finding Application (SoFiA) developed by Serra et al. (2015) to search through the entire GALFA-HI DR2 dataset for Leo T-like objects. SoFiA's user interface contains many optional input parameters and pre-processing choices. In this section, we enumerate the steps of our analysis before, during, and after running this program, along with our rationale.

1. We decided to search for sources only in velocity slices where the average brightness temperature was < 1 K, to avoid the brightest Galactic emission. For most data cubes this range was typically $\sim 40 \text{ km s}^{-1}$ wide centered around $V_{\text{LSR}} = 0 \text{ km s}^{-1}$, but for some cubes at lower Galactic latitude the range was as high as 175 km s^{-1} (see Figure 1). In addition, we removed the Galactic background emission from each data cube by applying an unsharp mask to each velocity slice. Without doing this, SoFiA would often merge discrete HI blobs at low to moderate V_{LSR} with the extended Galactic emission. After experimenting with various masks and finding no major differences in the properties of the sources SoFiA detected, we chose a mask radius of $r = 30$ arcmin. This radius is both larger than the expected size of a candidate galaxy, and consistent with the smoothing box size chosen by Saul et al. (2012) for searching the GALFA-HI DR1 data.
2. When running SoFiA we turned on the noise scaling filter which normalizes the input data cube by the local noise level in each velocity slice, thus preventing faint sources from being thrown out solely because they were being compared to a less noisy background. SoFiA measures local RMS noise by defining a box around each source, calculating the median absolute deviation of all pixels within that box that are not masked as part of the source, and multiplying by 1.4 under the assumption of Gaussian noise (T. Westmeier 2019, personal communication). The noise level varies across the sky, largely as a function of Galactic latitude; near the plane ($|b| < 15^{\circ}$), the average RMS noise level SoFiA calculates near detected sources is 0.21 K, while far from the plane ($b > 70^{\circ}$) it is 0.16 K.

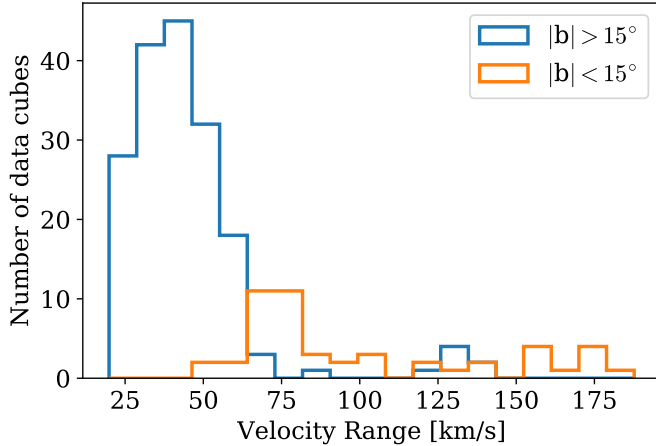


Figure 1. Distribution of Galactic emission region sizes in km s^{-1} with an average brightness temperature $T_{\text{B}} > 1 \text{ K}$ for all 225 data cubes, separated into regions of high and low Galactic latitude (b). We chose 1 K as a compromise between being able to push to lower velocities and being able to distinguish extended Galactic emission from compact sources.

3. For the source finding itself, we used the “Smooth+Clip” (S+C) finder, which smooths the data cube with user-inputted Gaussian kernels and then separates pixels that have a flux greater than some thresholds relative to the noise level. Pixels that were ≤ 1 pixel apart in

any dimension were merged into a single source. We chose a 4 pixel full width at half maximum (FWHM) for each spatial dimension to match the survey resolution, a 5, 10, 20, and 30 pixel ($3.68, 7.36, 14.72,$ and 22.08 km s^{-1}) FWHM for the velocity dimension to cover the potential ranges of velocity widths of yet undetected dwarf galaxies, and a 5σ flux threshold to reduce the probability of detecting too many spurious sources. If a source was found in any applied smoothing filter, it was then added to the catalog.

4. Once the source catalog for each cube was compiled, we removed previously known galaxies and then applied a series of cuts to remove any obviously spurious sources and tune our source list to most resemble dwarf galaxies. For reference, the properties of several recently discovered gaseous dwarf galaxies are shown in Table 1 (the definitions of the columns in the table are given in Section 3 except for M_* , the stellar mass in M_{\odot} , and D , the distance to the galaxy in Mpc). We set the minimum and maximum major axes of the ellipse fitted to the spatial extent of the source (called *ell3s_maj* in SoFiA) to 4 and 8 pixels, respectively; the minimum and maximum velocity widths (w_{50}) to 10 and 50 km s^{-1} , respectively; the maximum axis ratio of the source to 1.5; and the minimum integrated signal-to-noise ratio to 20.

Table 1. Properties of Recently Detected Local Group Galaxies with HI

Galaxy	R.A. (J2000)	Decl. (J2000)	l ($^{\circ}$)	b ($^{\circ}$)	F_{HI} (Jy km s^{-1})	M_{HI} ($10^5 M_{\odot}$)	M_* ($10^5 M_{\odot}$)	w_{50} (km s^{-1})	V_{LSR} (km s^{-1})	D (Mpc)
Leo T	09 ^h 34 ^m 53 ^s .4	17 [°] 03′05″	214.85	43.66	9.9	4.1	2.0	17	34	0.42
Leo P	10 ^h 21 ^m 45 ^s .1	18 [°] 05′17″	219.65	54.43	1.3	8.1	5.6	24	261	1.62
Pisces A	00 ^h 14 ^m 46 ^s .0	10 [°] 48′47″	108.52	-51.03	1.2	89	100	23	236	5.64
Pisces B	01 ^h 19 ^m 11 ^s .7	11 [°] 07′18″	133.83	-51.16	1.6	300	316	43	611	8.89

NOTE— The Leo T data are from Adams & Oosterloo (2018), the Leo P data are from McQuinn et al. (2015), and the Pisces A and B data are from Tollerud et al. (2016).

At the end of this process we were left with ~ 1000 HI sources. We did a final pruning of this source list by examining the moment maps and velocity spectra of each source by eye, and removing as candidates only those that were obviously artifacts or very close to the edge of their cube and were not already removed by the previous data cuts, or had irregular velocity spectra at high $|V_{\text{LSR}}|$. This process resulted

in a final list of 690 objects, the beginning of which is shown in Table 2. The entire list is provided in the online journal.

2.3. Optical Correlation

We developed and tuned an algorithm to recognize the stellar population of Leo T and other local dwarf galaxies from Pan-STARRS data, and then applied it to our HI candidates. The algorithm works as follows.

1. We draw a model population from a stellar isochrone of a given age and metallicity, downloaded from the CMD input form¹ (Bressan et al. 2012; Chen et al. 2014, 2015; Tang et al. 2014). We chose from isochrones with ages of 0.5, 2, 5, and 10 Gyr and metallicities of $[Fe/H] = -1, -1.5,$ and -2 to account for the large range of stellar properties of dwarfs.
2. We assign magnitudes to the model population by linearly interpolating the magnitudes and integrated IMF parameters of its isochrone, and then place it at a range of possible distances.
3. We assign magnitude and color errors based on the uncertainties provided by Pan-STARRS in the area around the source.
4. We compute the detection probability of the stars as a function of magnitude by binning the stars in the relevant Pan-STARRS field and fitting a power law. We then apply this detection probability to the model population.
5. We then compute the fraction of the model population that is within 1σ of a real star on both the magnitude and color axes.
6. To report a detection, we require a significant peak in the overlapping fraction as a function of distance relative to a nearby control field.

We tested this method on the resolved stellar population of the Draco Dwarf galaxy and easily recovered a distance within 10% of its measured distance of 76 kpc (McConnachie 2012). We were also able to detect Leo T with this method (Figure 2), though the measured distance is not very accurate. Of the three metallicities, the peak of the lowest metallicity isochrones (red lines) is closest to Leo T’s known distance (420 kpc), but the width is large. This indicates that Leo T’s distance is already approaching our algorithm’s detection limit when used with Pan-STARRS and that beyond that limit, further analysis would be required to confidently identify a stellar population.

In addition to fitting to stellar isochrones, we also visually inspected Pan-STARRS images at each source’s coordinates to identify any potential signs of a galaxy, because a galaxy’s stars may be resolved or unresolved depending on its distance. We obtained uniformly scaled images by combining the $y, i,$ and g filters downloaded from the image cutout server² with Astropy’s `make_lupton_rgb` function (Astropy

¹ <http://stev.oapd.inaf.it/cgi-bin/cmd>

² <http://ps1images.stsci.edu/cgi-bin/ps1cutouts>

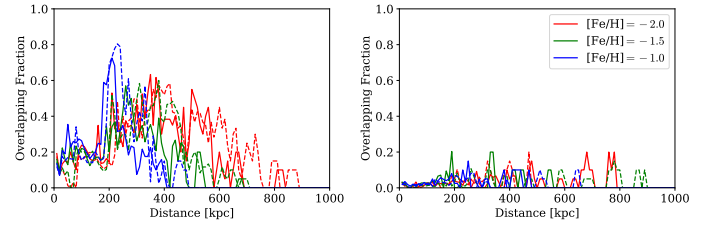


Figure 2. Fractions of model stellar populations that overlap with real stars in the Pan-STARRS field for Leo T, which is at a distance of ~ 420 kpc (left), and for the average of four control fields 10 and 20 arcmin away on either side of Leo T at the same Galactic latitude (right). Solid and dashed lines are 10 and 5 Gyr isochrones, respectively.

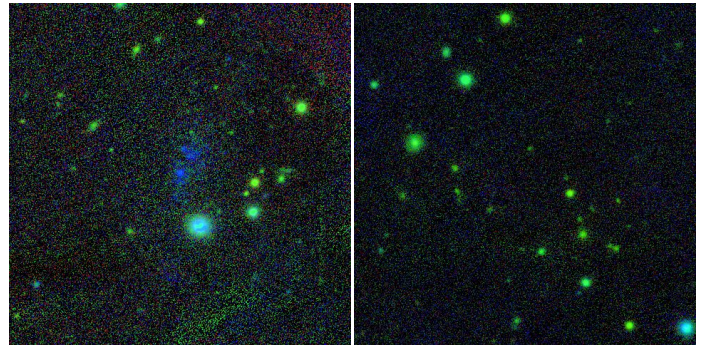


Figure 3. Leo P in Pan-STARRS (left) at a distance of 1.6 Mpc which represents what we would identify as a successful detection of diffuse blue light, compared to a nearby field without a galaxy (right). Both images are 2 arcmin across.

Collaboration et al. 2018) to detect any potential stellar populations, which would show up as diffuse blue light. Figure 3 shows a successful detection of Leo P using this method at a distance of 1.6 Mpc (McQuinn et al. 2015). Pan-STARRS also reveals the HI discovered galaxies Pisces A and B at 5.6 and 8.9 Mpc (Tollerud et al. 2016), respectively, as diffuse blue light; however, the quality of the images varies for individual sources. Leo T’s stellar population does not appear as diffuse light because it is much closer and resolved.

3. RESULTS

3.1. Catalog and Sample Properties

There are 690 HI galaxy candidates that were also inspected for an optical component with Pan-STARRS. The first 10 candidates are shown in Table 2; the entire table can be found in the online journal. The table properties are as follows.

1. (Source ID) A string containing (1) the Galactic longitude, (2) the Galactic latitude (both in degrees), and (3) the V_{LSR} velocity in km s^{-1} .
2. (R.A. and Decl.) The R.A. (hours, minutes, and seconds) and decl. (degrees, arcminutes, and arcseconds) in J2000 coordinates of the source’s flux-weighted center (in other words, the “center of flux” of all pixels defined to be part of the source). Previous work in the ALFALFA group has found the HI positions to be accurate to within 30 arcsec (Kent et al. 2008).
3. (Size) The major axis of the ellipse in arcmin fitted to all pixels in the source that are $\geq 3\sigma$ above the local noise level (called *ell3s_maj* in SoFiA). Every such pixel is given equal weight in this calculation.
4. (S/N) The signal-to-noise ratio integrated over the entire velocity spectrum.
5. (F_{int}) The flux of the source integrated over the entire velocity spectrum in Jy km s^{-1} . This was converted from the extracted SoFiA values in units of K channel using the following factor: $\frac{F_{\text{int}} [\text{Jy km s}^{-1}]}{F_{\text{int}} [\text{K channel}]} = \frac{2k_B\theta^2}{\lambda_{21}^2} \cos(\delta) \times 0.74 \frac{\text{km s}^{-1}}{\text{channel}} \times 10^{23}$, where $\theta = 1$ arcmin in radians, $\lambda_{21} = 21.106$ cm, and δ is the source’s decl.
6. (T_B) The peak brightness temperature in K (called *f_peak*, the peak flux density in SoFiA).
7. (w_{50}) The line width at 50% of the peak flux density of the source in km s^{-1} .
8. (V_{LSR}) The local standard of rest velocity at the source’s flux-weighted center in km s^{-1} .

Table 2. Partial Source List Sorted by Increasing Galactic Longitude

Source ID	R.A.	Decl.	Size	S/N	F_{int}	T_B	w_{50}	V_{LSR}
($l+b+V_{\text{LSR}}$)	(h:m:s)	($^{\circ}:'''$)	(arcmin)		(Jy km s^{-1})	(K)	(km s^{-1})	(km s^{-1})
000.12+75.05-034	13:44:18	18:25:34	5.0	44	0.83	0.59	18	-34
000.68+72.41-029	13:53:26	16:55:19	4.2	36	0.64	0.5	18	-29
001.51+59.47+015	14:35:36	09:02:07	5.0	40	1.31	1.03	20	15
002.70+70.81-035	14:00:19	16:27:45	5.2	64	1.41	0.81	12	-35
003.89+68.38-062	14:09:29	15:21:07	7.3	80	3.14	0.98	14	-62
004.01+54.40-050	14:54:58	06:54:13	6.1	69	3.17	1.05	21	-50
004.27+57.23-059	14:46:19	08:46:05	5.8	51	1.61	1.0	13	-59
004.43+41.74-050	15:35:23	-00:45:48	5.5	70	1.98	0.75	15	-50
004.46+58.24-068	14:43:19	09:27:47	4.8	38	0.93	0.83	12	-68
006.80+58.39-028	14:45:50	10:32:03	4.6	35	0.75	0.58	11	-28

NOTE— Uncertainty estimates for each column are given in Section 3.1.

We now comment on the properties of our sample. In Figure 4 we see that sources are present over the entire DR2 field roughly uniformly, with a noticeable gap near R.A. $\approx 180^{\circ}$ corresponding to the North Galactic Pole. Sources are also present over a wide range of Galactic latitudes, notably including close to the Galactic plane ($|b| \lesssim 15^{\circ}$). The variation of the local noise calculated by SoFiA when searching the data is clearly dependent on Galactic latitude (lower latitudes have systematically higher RMS values) which affects the detection limit, as discussed below. However, the distribution of the HI sources across position and velocity space shows that the noise variation is not significantly dependent

on velocity. A majority ($\approx 75\%$) of sources have $|V_{\text{LSR}}| < 100 \text{ km s}^{-1}$, and we see structure at $V_{\text{LSR}} < -200 \text{ km s}^{-1}$ most likely associated with the Magellanic Stream.

Figure 5 shows a series of properties of our detected sources. The top panel demonstrates that we are detecting objects within our desired angular size range roughly uniformly, with a slight bias to smaller objects. At a distance of 500 kpc, these sizes correspond to diameters of 0.6–1.2 kpc. The upper middle panel shows that our upper limit on the velocity width of 50 km s^{-1} was conservative; nearly all sources have a velocity width $< 20 \text{ km s}^{-1}$. The plot also implies that the population would continue to lower velocity widths if we did not apply a cut at $w_{50} = 10 \text{ km s}^{-1}$. In examining the ve-

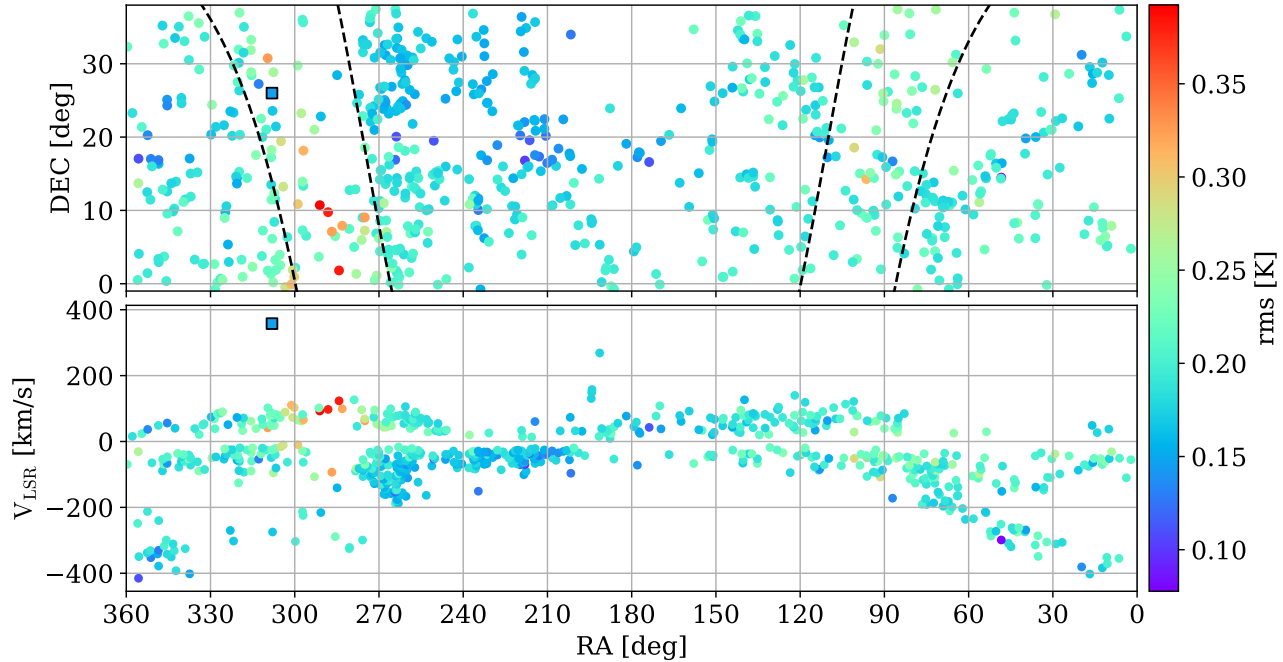


Figure 4. Top: R.A. and Decl. positions of each source. The regions within the dashed black lines correspond to the Galactic plane in between latitudes -15° and 15° . Bottom: local standard of rest velocity in km s^{-1} vs. R.A. for each source. Points are colored by their local RMS values calculated by SoFiA. The outlined square is the local volume candidate described in Section 3.4.

locity distribution (lower middle panel) we find that there is an overall bias toward objects with negative velocities; the median value of V_{LSR} is -46 km s^{-1} .

Fluxes range from 0.5 to $15.6 \text{ Jy km s}^{-1}$, and we show the distribution of fluxes in the bottom panel of Figure 5. The flux distribution turns over at 1.4 Jy km s^{-1} , but we note that the variability of the RMS values shown in Figure 4 implies that this turnover is not constant across the entire GALFA-HI field. At lower Galactic latitudes, the mean noise level is $\approx 10\%$ higher than the noise level outside of the plane. There are also known to be sources at lower fluxes than we detected in DR2 (see Saul et al. (2012) and Figure 7).

We estimated errors on the properties derived by SoFiA using injected sources, described in Section 3.2. Position uncertainties were on the order of 15 arcsec (negligible compared to the beam size), and velocity uncertainties were on the order of 1 km s^{-1} , or roughly 1-2 channel spacings. Fractional uncertainties were 2–8% for size measurements, 5–10% for w_{50} measurements, and 10–20% for all other reported parameters, depending on both the distance and the velocity the injected sources were placed at. Sources at larger distances and lower velocities had higher fractional uncertainties by as much as a factor of 3.

3.2. HI Detection Limits

We measure the value of the turnover in the flux distribution to be 1.4 Jy km s^{-1} . We convert this to a completeness limit estimate of $D_{\text{max}} = 1.74 \times \left(\frac{M_{\text{HI}}}{10^6 M_\odot}\right)^{1/2} \text{ Mpc}$ for an object with an HI-mass (M_{HI}) in solar masses. For an object with an HI-mass comparable to Leo T, this distance limit is $\sim 1.15 \text{ Mpc}$. If we compute D_{max} for the galaxies in Table 1, we find that Pisces A, B, and Leo P are all very close to their edge of detectability, and only Leo T itself is comfortably detectable. SoFiA was indeed easily able to find Leo T in the DR2 data, but it was unable to find Pisces A, Pisces B, or Leo P. However, we were able to find Pisces A in the DR2 data cube by manually applying smoothing filters.

Due to the inherent variability of backgrounds and foregrounds across the field, we ran further tests to better quantify our estimated detection limits. We injected 3D Gaussian sources³ meant to replicate Leo T’s accepted size and velocity width as found in Adams & Oosterloo (2018) (which are also consistent with the SoFiA-derived size and velocity width of 6.1 arcmin and 15 km s^{-1} , respectively) into each cube with a peak flux corresponding to Leo T’s actual distance (0.42 Mpc) at three different velocities: high velocity (250 km s^{-1}), a low velocity defined as 15 km s^{-1} greater than

³ Leo T’s actual HI profiles are not exactly Gaussian (Adams & Oosterloo 2018) so this assumption does lead to differences from Leo T’s accepted mass and flux by as much as a factor of 2.

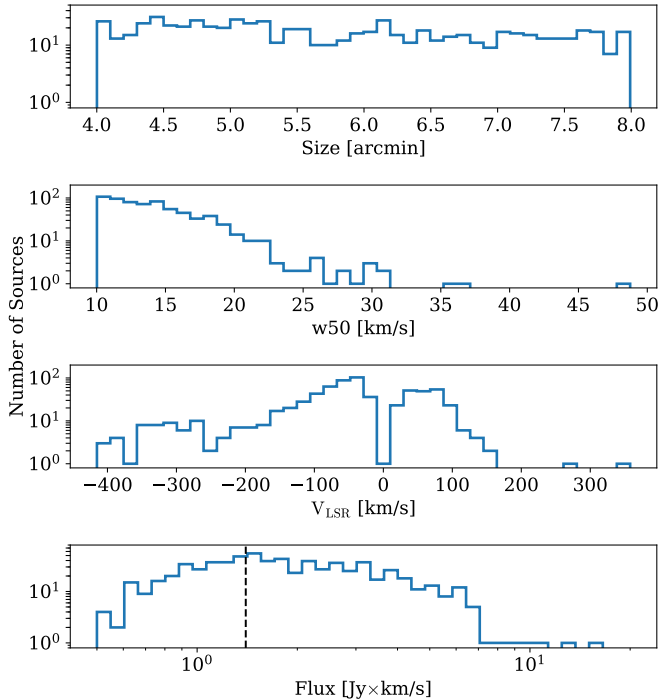


Figure 5. Distributions of angular size (top) in arcmin, velocity width (upper middle) in km s^{-1} , local standard of rest velocity (lower middle) in km s^{-1} , and integrated flux (bottom) in Jy km s^{-1} . The dashed line in the bottom panel is the estimated turnover of the flux distribution at 1.4 Jy km s^{-1} .

the boundary of the searched region defined in Section 2.2, and Leo T’s velocity (from Table 1). For the purpose of this test, we defined a successful detection to be one where SoFiA pulled out the injected source at its given velocity (within 15 km s^{-1}), position (within 5 arcmin), and derived a velocity width and size within our cuts used in Section 2.2. We recovered every injected source at high velocities, where Galactic emission is the weakest, and nearly every source at low velocities and Leo T velocities (97% and 82% respectively), the latter of which is lower because Leo T’s velocity is often within the region of average Galactic emission $> 1\text{K}$ which we purposely ignored. Nevertheless, we can confidently say that SoFiA would successfully detect Leo T at its actual distance in the vast majority of our search area.

We next wanted to determine how accurate our detection limit of Leo T-like objects was, based on our observed flux distribution. To do this, we performed the same procedure as before with two alterations; we scaled the peak flux of the injected source to a larger distance (from 0.5 to 1 Mpc) and we reduced the size of the injected source to better correspond to a more distant galaxy. At high velocities, the detection fraction dropped to its lowest value of 86% at 1 Mpc, but the

Table 3. Detection Fraction of Sources Injected at or beyond a Distance of 500 kpc

Mass (Leo T)	Distance (Mpc)	High- v	Low- v	Leo T- v
1	0.5	100%	76%	69%
1	0.75	99%	40%	45%
1	1	86%	11%	18%
2	1	100%	46%	50%
3	1	100%	68%	63%
10	1	100%	83%	76%

NOTE— The HI mass of Leo T is $4.1 \times 10^5 M_{\odot}$. Detection fractions are colored and shaded by how far above (green) or below (red) 50% they are.

difference at low and Leo T velocities is much more drastic, as shown in the first three rows of Table 3 (with Mass = 1 Leo T). Note, however, that a typical local group galaxy that is 1 Mpc away has a velocity closer to our high-velocity case than either of the lower-velocity cases. In other words, the region of distance-velocity space where our detection fraction is lowest also probably contains the smallest number of dwarf galaxies. We also tried reducing the injected sources’ size, which results in a $\sim 10\%$ drop in the detection fraction at lower velocities compared to the same test without changing the size, meaning the dominant reason for the overall drop is the reduction in flux caused by increasing distance. In the bottom three rows of Table 3 we inject sources with successively larger multiples of Leo T’s mass to determine how complete we are out to 1 Mpc. We note that we would detect $\approx 50\%$ of galaxies at lower velocities with only 2 times Leo T’s mass, and $\approx 66\%$ of those with 3 times Leo T’s mass.⁴

The last row of 10 times Leo T’s mass is an exception to the previous rows in that the size and w_{50} cuts we apply are the dominant cause for reduction in recovered sources in regions significantly contaminated by Galactic emission at low velocities. Without the size and w_{50} cuts, the detection fractions are all $> 92\%$. The higher level of background noise at low latitude causes SoFiA to chop off the outer regions of the object in its size calculation. Therefore our size cut may lead us to miss some dwarf galaxies with a range of HI masses at low latitudes and velocities.

3.3. Optical Results

Using the algorithm defined in Section 2.3 we also attempted to find optical counterparts for all of our sources.

⁴ At 4 times Leo T’s mass we naturally recover the same detection fractions as the first row of Table 3, because multiplying the mass of the third row by 4 is equivalent to halving the third row’s distance in terms of HI flux.

Table 4. HI properties of Local Volume candidate shown in Figure 6

Parameter	LV Candidate
Source ID ($l+b+V_{\text{LSR}}$)	067.73-08.13+358
R.A. (J2000)	20 ^h 32 ^m 26 ^s
Decl. (J2000)	25°59'46''
Size (arcmin)	4.4
S/N	175
F_{int} (Jy km s ⁻¹)	4.97
T_B (K)	1.44
w_{50} (km s ⁻¹)	49
V_{LSR} (km s ⁻¹)	358

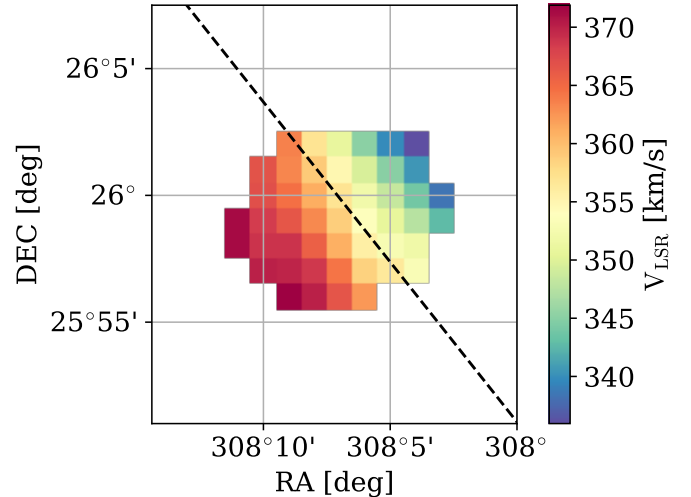
The vast majority of overlapping fractions were no larger than those of nearby control fields, and the few that were larger were not at all comparable to the values seen in the left panel of Figure 2, indicating no resolvable stellar populations. We note that Leo T is already close to the edge of detectability in Pan-STARRS and it is only ≈ 400 kpc away, so it is not necessarily surprising we were unable to see a stellar population in any of our HI sources of potentially comparable HI-masses out to 1 Mpc. We also checked the Pan-STARRS fields visually, as described in Section 2.3, and found two potential sources with diffuse blue light (see Appendix), but otherwise nothing that indicated an unresolved stellar population similar to Leo P shown in Figure 3.

3.4. Local Volume Candidate

In Table 4 we show the properties of a particularly unusual galaxy candidate that is very close to the Galactic plane ($b = -8^\circ$) in the constellation Vulpecula. It is an outlier in our sample in many respects. As evident in Figure 4, it has the largest positive value of V_{LSR} , and is the only object in our sample with $V_{\text{LSR}} > 300$ km s⁻¹. It has a much larger signal-to-noise ratio than the typical value of ≈ 65 for our source list. Its velocity width is just below our cutoff at 50 km s⁻¹ and at the tail end of the distribution of velocity widths which has a mean of ≈ 15 km s⁻¹ (see Figure 5). We also note that it is in an area of the sky not covered by DR1 or ALFALFA. Figure 6, a velocity moment map of this source, shows evidence for a velocity gradient. Follow-up optical imaging suggests a faint optical counterpart, to be detailed in a forthcoming paper.

4. COMPARISON TO OTHER CATALOGS

We find broad consistencies in the properties of our sources compared to the Compact Cloud Catalog based on GALFA-HI's DR1 data (Saul et al. 2012) and objects in the ALFALFA survey (Haynes et al. 2018) categorized as high velocity

**Figure 6.** HI velocity map of the local volume candidate in (R.A., decl.) coordinates. Surrounding (unconnected) pixels have been masked out. The dashed line is Galactic latitude $b = -8.13^\circ$.

clouds (HVCs). For comparison to the ALFALFA catalog we used the $\alpha - 100$ complete catalog available on their website⁵, which they state is not fully vetted but which contains Galactic sources not included in Haynes et al. (2018). We found sources in common between the surveys distributed uniformly across all areas of overlap on the sky. For a match, we required the difference in both R.A. and decl. to be < 5 arcmin, and the difference in the center of the velocity spectrum to be < 15 km s⁻¹. We do not recover all sources from Saul et al. (2012) or ALFALFA (68 matching objects in the former, 47 matching objects in the latter) due to differing search parameter choices and catalog methods, survey depths, and ALFALFA's lower velocity resolution. Our sky-coverage also for the first time includes the Galactic plane.

Comparisons of the same distributions in Figure 5 for the compact cloud and ALFALFA catalogs are shown in Figure 7. Our velocity width distribution (top panel) does not extend over the same range as Saul et al. (2012)'s because we cut off sources with $w_{50} < 10$ km s⁻¹ and applied different masks when searching the data to focus on potential galaxy sources over clouds. Our sources extend over the velocity widths of both the cold ($\Delta V < 15$ km s⁻¹) and warm ($\Delta V > 15$ km s⁻¹) clouds defined by Saul et al. (2012). The difference between our catalog and the ALFALFA distribution also comes partially from the search masks we apply, but at the lower width end it is due to ALFALFA's much larger channel spacing of 5 km s⁻¹. Our sources have cen-

⁵ <http://egg.astro.cornell.edu/alfalfa/data/>

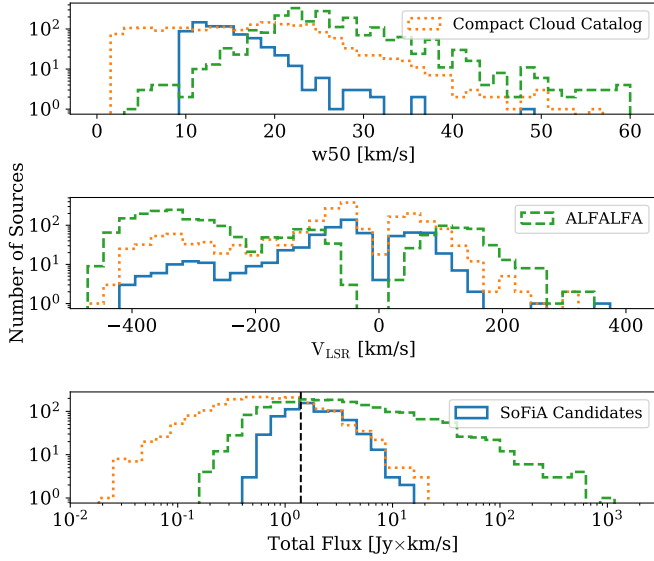


Figure 7. Distributions of velocity width (top) in km s^{-1} , local standard of rest velocity (middle) in km s^{-1} , and integrated flux (bottom) in Jy km s^{-1} for our sources (solid blue), the Compact Cloud Catalog (dotted orange), and HVCs from ALFALFA (dashed green). The dashed black line in the bottom panel is the estimated turnover of our flux distribution at 1.4 Jy km s^{-1} , the same as in Figure 5.

tral velocities (middle panel) that follow the distribution of Saul et al. (2012) very closely and have the same median $V_{\text{LSR}} \approx -50 \text{ km s}^{-1}$. The ALFALFA HVCs have more negative velocities (median $V_{\text{LSR}} \approx -300 \text{ km s}^{-1}$) most likely due to their catalog capturing many large clouds, such as those associated with the Magellanic system.

Saul et al. (2012)’s flux distribution is essentially identical to ours down to 1.4 Jy km s^{-1} , though it continues to nearly two orders of magnitude fainter in flux. This is to be expected as DR1 was deeper in some areas of the sky and therefore able to pick out fainter sources. The ALFALFA catalog has a similar turnover but includes many more sources at higher fluxes, again due to the lack of size or velocity width cuts.

In Figure 8, we directly compare properties of our candidates, the Compact Cloud Catalog, and the four reference dwarf galaxies from Table 1. The left panel shows the HI-masses of our candidates and objects in the Compact Cloud Catalog all placed at 1 Mpc. We see that both Leo T and Leo P have comparable HI-masses compared to the derived masses of our candidates if placed at 1 Mpc. Though the right panel implies dwarf galaxies are more likely to have large positive values of V_{LSR} , Leo T’s existence demonstrates that local dwarfs can also have low velocities.

5. DISCUSSION

5.1. Local Volume Candidate

There is an observed dearth of MW satellites and local group galaxies at low Galactic latitudes (see Figure 1 of McConnell 2012), presumably due to the difficulties of detecting anything in the crowded Galactic plane. If confirmed, our local volume candidate would begin to fill in the spatial distribution of nearby dwarf galaxies in regions the Galactic plane obscures. Using the galaxy candidate’s measured integrated flux, we calculate it to have a HI-mass of $1.17 \left(\frac{D}{1 \text{ Mpc}}\right)^2 \times 10^6 M_{\odot}$, where D is its as yet undetermined distance. It has a velocity width similar to Pisces B, which was also first discovered in GALFA data, and if it also has a similar HI-mass, its HI-flux would place it at a distance of $\approx 5 \text{ Mpc}$ (see Figure 8). This is also very close to the distance we derive assuming the candidate is in the Hubble flow ($D = V_{\text{LSR}}/H_0$, where $H_0 = 70 \text{ km s}^{-1} \text{ Mpc}^{-1}$). Using an estimate of the dynamical mass, $M_{\text{dyn}} = 6.2 \times 10^3 a W_{50}^2 d$ (Equation (8) from Adams et al. (2013)), where a is the angular diameter in arcmin, W_{50} is the velocity width in km s^{-1} , and d is the distance Mpc, we calculate a dynamical mass from our HI data of $6.5 \left(\frac{D}{1 \text{ Mpc}}\right) \times 10^7 M_{\odot}$. If $D = 5 \text{ Mpc}$, we derive an HI-mass-to-total mass ratio of 0.1. We defer further analysis of this object’s physical properties to a future paper with optical follow-up, which will in particular allow us to measure its distance. However, we speculate here that it is very unlikely our candidate is as close as Leo T due to its large velocity, which is inconsistent with other known galaxies in the local group (McConnell 2012), and the absence of a Leo T-like optical image from Pan-STARRS: thus, it is probably not a true Leo T analog.

5.2. Dwarf Galaxy Limits

We discuss our limits on dwarf galaxy candidates in two regimes: a galactocentric distance $< 500 \text{ kpc}$ and a galactocentric distance $> 500 \text{ kpc}$. We can place our strongest constraints on the existence of Leo T-like objects in the first regime, where both gas from GALFA-HI and resolved stellar populations in Pan-STARRS are detectable (see Section 2). The fact that we do not see stellar populations in any of our candidates shows that there are no other Leo T-like objects closer than 500 kpc within the GALFA-HI footprint, except possibly near the Galactic plane (where the stellar population would be indistinguishable from foreground stars) or near $V_{\text{LSR}} = 0 \text{ km s}^{-1}$ (where we did not search to avoid bright Galactic emission). This nondetection is not completely surprising, as ram pressure stripping and other mechanisms near the MW (at $\sim 250 \text{ kpc}$) are expected to deplete the gas in dwarfs that reside there (Grcevich & Putman 2009; Nichols & Bland-Hawthorn 2011; Spekkens et al. 2014; Emmerick et al. 2016). Nevertheless, there remains a volume of $\approx 0.17 \text{ Mpc}^3$ (the GALFA-HI sky out to 500 kpc) where we detect no additional Leo T-like objects. Our nondetection

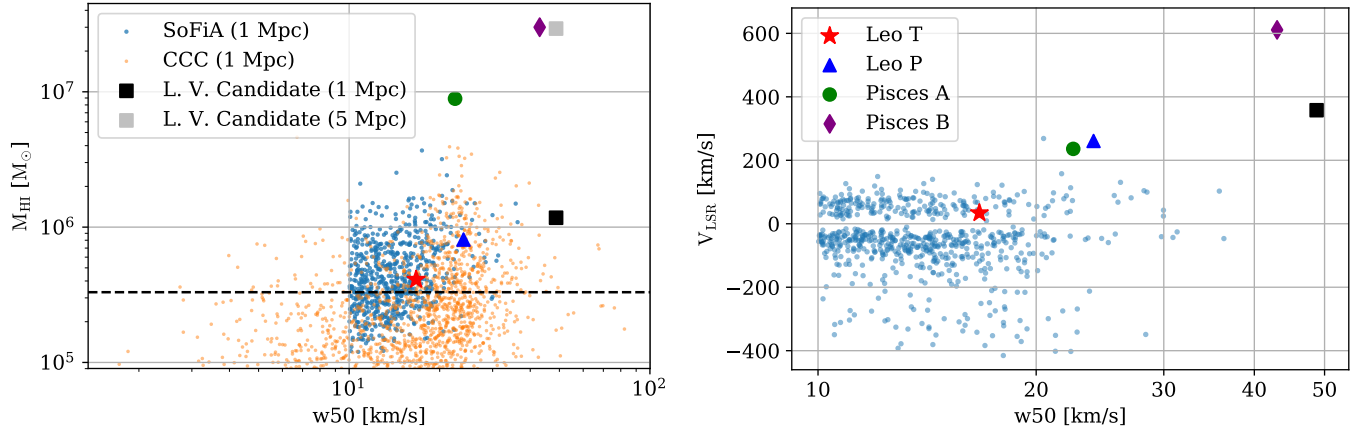


Figure 8. Left: HI-mass in M_{\odot} vs. velocity width (w_{50}) in km s^{-1} . The blue and orange points are our candidate sources and objects in the Compact Cloud Catalog, respectively. They are all placed at a constant distance (1 Mpc) to derive an HI-mass. The dashed line is the HI-mass corresponding to a flux of 1.4 Jy km s^{-1} , also at 1 Mpc. Right: local standard of rest velocity in km s^{-1} vs. w_{50} for our sources. Also shown in both panels are the four galaxies in Table 1, and our local volume candidate placed at a possible distance of 1 and 5 Mpc.

within this distance is consistent with a reionization epoch during which gas is removed from dwarf galaxies in the local group with halo masses $\lesssim 10^{8.5} M_{\odot}$ (Tollerud & Peek 2018). In summary, an object like Leo T appears to be a rarity < 500 kpc from the MW in the GALFA-HI footprint (which covers one-third of the sky), rather than one of many such objects.

At distances > 500 kpc, we are unable to detect resolved stellar populations in Pan-STARRS, and our ability to detect Leo T-mass objects is significantly reduced at lower velocities. We can detect Leo T-like objects in HI at high velocities clear of background emission at 1 Mpc, but we only have that same level of completeness at low velocities for sources with 10 times Leo T’s mass at 1 Mpc. More distant objects with larger stellar populations than Leo T can be detected as diffuse blue light in Pan-STARRS (e.g. as Leo P appears in Figure 3), and we inspected the data for these optical sources. Though we have not quantified the distance range and stellar population detectable as diffuse blue light in Pan-STARRS, the lack of any visual detections is consistent with all of our candidates’ stellar masses being less than Leo P’s stellar mass of $5.6 \times 10^5 M_{\odot}$ at a distance of 1.62 Mpc. Therefore, despite the fact that many of our candidates would be comparable in HI-mass to Leo P at distances $\gtrsim 1$ Mpc (see Figure 8), the general lack of diffuse blue light is not encouraging that a large number of these are new galaxies. It also remains possible that some of our candidates are dark matter halos that just contain HI, as gas-rich minihalos without stars are predicted to exist around the MW (Ricotti 2009).

If we consider our results in the context of the missing satellites problem (Klypin et al. 1999) as well as more re-

cent galaxy count mismatches in the local field (Klypin et al. 2015), we see that they support a model of strong and effective reionization that limits star formation in satellites at later times. However, the precise mechanism that operates during reionization is not yet clear. Both Brown et al. (2014) and Tollerud & Peek (2018) invoke reionization from massive stars in early galaxies to explain the current population of local dwarfs; the former by measuring ancient stellar populations, and the latter by setting a halo mass at which a dwarf cannot retain gas. Our lack of detections of Leo T-like objects strengthens this interpretation. We note though that when looking directly at star-formation histories, Weisz et al. (2014) could not conclusively determine the effect reionization had, if any, on local dwarfs, meaning more observations are necessary to be able to distinguish between reionization models.

Finally, we consider what other classifications for our HI sources are possible besides small galaxies. In Figure 9, we compare our candidates to objects in the Compact Cloud Catalog of Saul et al. (2012). For the 68 matches between the two, we see a strong overlap between different types of clouds; our candidate list contains objects that overlap all types of HI sources identified in Saul et al. (2012), including high-velocity clouds, cold and warm low-velocity clouds, and galaxy candidates far from known HI complexes. Therefore, a plausible scenario is that most of these HI sources are a heterogeneous mixture of nearby MW structures. However, we note that it is possible that galaxies sitting at the outskirts of the local group may have small velocities (like Leo T) and could have been identified as a low-velocity cloud in Saul et al. (2012).

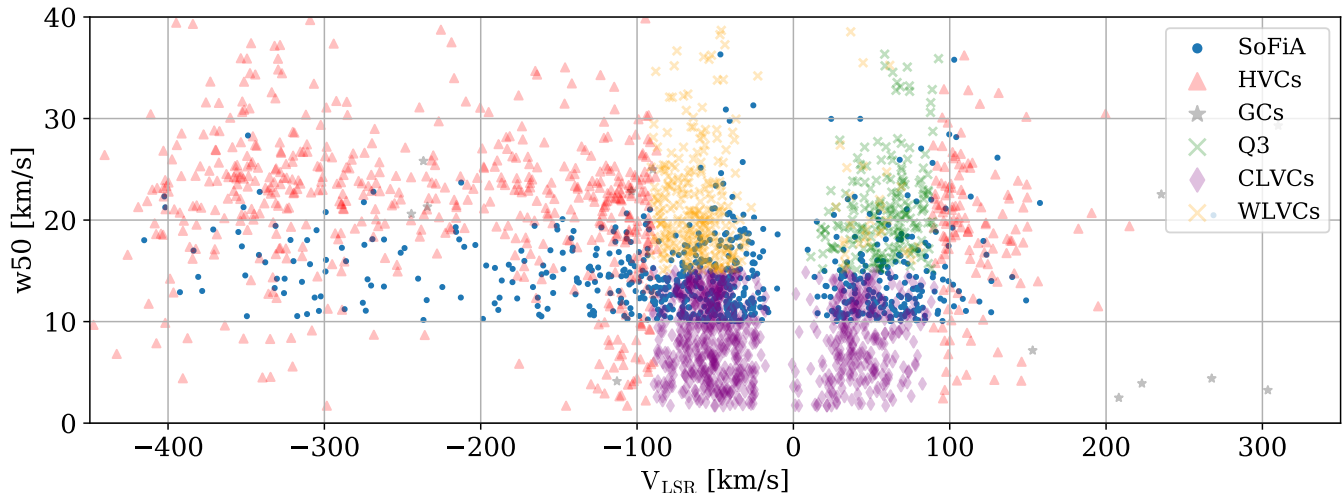


Figure 9. Velocity width vs. local standard of rest velocity for SoFiA candidates and Compact Cloud Catalog objects, the latter of which is separated into HVCs which are near known complexes and have $|V_{\text{LSR}}| > 90 \text{ km s}^{-1}$, galaxy candidates (GCs) not near known complexes with $|V_{\text{LSR}}| > 90 \text{ km s}^{-1}$, cold low-velocity clouds (CLVCs) with $|V_{\text{LSR}}| < 90 \text{ km s}^{-1}$ and $w_{50} < 15 \text{ km s}^{-1}$, warm low-velocity clouds (WLVCs) with $|V_{\text{LSR}}| < 90 \text{ km s}^{-1}$ and $w_{50} > 15 \text{ km s}^{-1}$, and Q3 WLVCs with $0 < V_{\text{LSR}} < 90 \text{ km s}^{-1}$, $w_{50} > 15 \text{ km s}^{-1}$, and $180^\circ < l < 270^\circ$.

6. SUMMARY

Using Data Release 2 of GALFA-HI we performed a search for new local dwarf galaxies. We found 690 candidates, among which is an extremely promising candidate in the Galactic plane that is likely within the local volume at $V_{\text{LSR}} = 358 \text{ km s}^{-1}$. We quantified our completeness by injecting Leo T-like sources into each GALFA-HI data cube and measuring the fraction of sources detected by SoFiA. We found we were complete out to 1 Mpc at high velocities and out to Leo T’s distance at low velocities for Leo T-like dwarfs. We searched Pan-STARRS for resolved stellar populations and found none comparable to Leo T’s, thus ruling out the existence of other Leo T-like dwarfs within the GALFA-HI footprint at distances $< 500 \text{ kpc}$, except possibly at the lowest Galactic latitudes and local standard of rest velocities. We also searched for unresolved stellar populations manifesting as diffuse blue light in Pan-STARRS images, but again found no evidence of any, which limits the number of more

massive dwarfs in the vicinity of the local group. We conclude that our results are consistent with strong reionization effects on the evolution of dwarf galaxies. Finally, we highlight some of our strongest candidates for potential follow-up observations in the Appendix.

We thank the entire GALFA team, and in particular Josh Peek, Yong Zheng, and Susan Clark for their help with the analysis of the GALFA-HI data and for useful discussions. We also thank Tobias Westmeier for assistance with interpreting the output from SoFiA, and the anonymous referee for helpful comments. M.E.P. acknowledges support from the National Science Foundation under grant No. AST-1410800.

Software: This research made use of Astropy, a community-developed core Python package for Astronomy (Astropy Collaboration et al. 2018), the open-source software tools Numpy, Matplotlib, and IPython (Hunter 2007; Perez & Granger 2007; van der Walt et al. 2011), and the SoFiA source finding pipeline (Serra et al. 2015).

REFERENCES

- Adams, E. A. K., Giovanelli, R., & Haynes, M. P. 2013, *ApJ*, 768, 77
- Adams, E. A. K., & Oosterloo, T. A. 2018, *A&A*, 612, A26
- Astropy Collaboration, Price-Whelan, A. M., Sipőcz, B. M., et al. 2018, *AJ*, 156, 123
- Bechtol, K., Drlica-Wagner, A., Balbinot, E., et al. 2015, *ApJ*, 807, 50
- Belokurov, V., Zucker, D. B., Evans, N. W., et al. 2006, *ApJL*, 647, L111
- . 2007, *ApJ*, 654, 897
- Bressan, A., Marigo, P., Girardi, L., et al. 2012, *MNRAS*, 427, 127
- Brown, T. M., Tumlinson, J., Geha, M., et al. 2014, *ApJ*, 796, 91
- Chambers, K. C., Magnier, E. A., Metcalfe, N., et al. 2016, *ArXiv e-prints*, arXiv:1612.05560 [astro-ph.IM]

- Chen, Y., Bressan, A., Girardi, L., et al. 2015, *MNRAS*, 452, 1068
- Chen, Y., Girardi, L., Bressan, A., et al. 2014, *MNRAS*, 444, 2525
- Donovan Meyer, J., Peek, J. E. G., Putman, M., & Grcevich, J. 2015, *ApJ*, 808, 136
- Emerick, A., Mac Low, M.-M., Grcevich, J., & Gatto, A. 2016, *ApJ*, 826, 148
- Fritz, T. K., Battaglia, G., Pawlowski, M. S., et al. 2018, *A&A*, 619, A103
- Garrison-Kimmel, S., Hopkins, P. F., Wetzel, A., et al. 2019, *MNRAS*, 487, 1380
- Grcevich, J., & Putman, M. E. 2009, *ApJ*, 696, 385
- Hargis, J. R., Willman, B., & Peter, A. H. G. 2014, *ApJL*, 795, L13
- Haynes, M. P., Giovanelli, R., Kent, B. R., et al. 2018, *ApJ*, 861, 49
- Hunter, J. D. 2007, *CSE*, 9, 90
- Irwin, M. J., Belokurov, V., Evans, N. W., et al. 2007, *ApJL*, 656, L13
- Kent, B. R., Giovanelli, R., Haynes, M. P., et al. 2008, *AJ*, 136, 713
- Klypin, A., Karachentsev, I., Makarov, D., & Nasonova, O. 2015, *MNRAS*, 454, 1798
- Klypin, A., Kravtsov, A. V., Valenzuela, O., & Prada, F. 1999, *ApJ*, 522, 82
- McConnachie, A. W. 2012, *AJ*, 144, 4
- McQuinn, K. B. W., Skillman, E. D., Dolphin, A., et al. 2015, *ApJ*, 812, 158
- Newton, O., Cautun, M., Jenkins, A., Frenk, C. S., & Helly, J. C. 2018, *MNRAS*, 479, 2853
- Nichols, M., & Bland-Hawthorn, J. 2011, *ApJ*, 732, 17
- Peek, J. E. G., Heiles, C., Douglas, K. A., et al. 2011, *ApJS*, 194, 20
- Peek, J. E. G., Babler, B. L., Zheng, Y., et al. 2018, *ApJS*, 234, 2
- Perez, F., & Granger, B. E. 2007, *CSE*, 9, 21
- Ricotti, M. 2009, *MNRAS*, 392, L45
- Ricotti, M., & Gnedin, N. Y. 2005, *ApJ*, 629, 259
- Ricotti, M., Parry, O. H., & Gnedin, N. Y. 2016, *ApJ*, 831, 204
- Saul, D. R., Peek, J. E. G., Grcevich, J., et al. 2012, *ApJ*, 758, 44
- Serra, P., Westmeier, T., Giese, N., et al. 2015, *MNRAS*, 448, 1922
- Simon, J. D., & Geha, M. 2007, *ApJ*, 670, 313
- Spekkens, K., Urbancic, N., Mason, B. S., Willman, B., & Aguirre, J. E. 2014, *ApJL*, 795, L5
- Tang, J., Bressan, A., Rosenfield, P., et al. 2014, *MNRAS*, 445, 4287
- Tollerud, E. J., Bullock, J. S., Strigari, L. E., & Willman, B. 2008, *ApJ*, 688, 277
- Tollerud, E. J., Geha, M. C., Grcevich, J., et al. 2016, *ApJ*, 827, 89
- Tollerud, E. J., & Peek, J. E. G. 2018, *ApJ*, 857, 45
- van der Walt, S., Colbert, S. C., & Varoquaux, G. 2011, *CSE*, 13, 22
- Walsh, S. M., Willman, B., & Jerjen, H. 2009, *AJ*, 137, 450
- Weisz, D. R., Dolphin, A. E., Skillman, E. D., et al. 2014, *ApJ*, 789, 148
- Willman, B., Dalcanton, J. J., Martinez-Delgado, D., et al. 2005, *ApJL*, 626, L85
- Zucker, D. B., Belokurov, V., Evans, N. W., et al. 2006, *ApJL*, 650, L41

APPENDIX

Table 5 lists the most promising candidates in our catalog for potential follow-up based on their HI and/or optical properties. The sources marked with a *B* are potentially associated with diffuse blue light offset from the center of the HI source by $\lesssim 3$ arcmin. The source marked with a *V* is isolated in velocity space as the only source other than the Local Volume candidate with $V_{\text{LSR}} > 200 \text{ km s}^{-1}$. All of the other sources have velocity widths larger than that of Pisces A ($w_{50} > 22.5 \text{ km s}^{-1}$). Velocity maps of these sources are shown in Figure 10.

Table 5. Promising Candidates to Target for Potential Follow-up Observations, Sorted by Increasing Galactic Longitude

#	Source ID ($l+b+V_{\text{LSR}}$)	R.A. (h:m:s)	Decl. ($^{\circ}:'''$)	Size (arcmin)	S/N	F_{int} (Jy km s^{-1})	T_B (K)	w_{50} (km s^{-1})	V_{LSR} (km s^{-1})
1	024.86+24.05+068	17:11:31	04:06:42	5.2	57	2.16	0.91	26	68
2	041.87-14.92+103	20:00:41	00:55:55	7.2	104	6.32	1.68	36	103
3	046.10-09.25+082	19:48:46	07:17:17	6.1	82	3.78	0.99	27	82
4	047.56+27.33-043	17:32:58	24:08:54	6.5	80	2.39	0.89	31	-43
5	050.68-19.13-026	20:32:08	06:08:02	6.6	60	2.62	1.05	31	-26
6	052.97+33.93-041	17:10:32	30:29:55	5.8	58	1.25	1.02	30	-41
7	063.19+22.95-032	18:12:46	36:12:26	6.0	71	2.59	0.91	26	-32
8	063.94+24.91-045	18:04:25	37:26:22	4.1	43	0.93	0.88	24	-45
9	073.70-11.75-059	21:01:30	28:25:59	5.4	56	1.8	0.93	25	-59
10	083.17-44.66-047	23:01:32	09:33:36	7.4	87	4.61	1.06	36	-47
11	^B 084.85-40.49-351	22:55:57	13:41:39	4.1	45	0.97	0.88	15	-351
12	085.14-55.33-212	23:29:48	01:26:26	6.2	94	4.17	1.05	24	-212
13	092.06-40.55-341	23:15:28	16:30:01	7.2	96	3.62	0.85	23	-341
14	^B 110.15-29.23-069	23:58:36	32:19:32	6.1	46	1.27	0.88	18	-69
15	154.71-36.35-269	02:38:37	19:49:10	6.6	81	2.82	0.71	23	-269
16	155.71-46.33-349	02:20:54	10:45:56	6.7	70	3.33	1.18	28	-349
17	197.33+00.91-046	06:25:43	14:16:26	4.8	119	6.34	1.9	25	-46
18	201.91-01.75-050	06:24:51	08:59:15	6.5	109	5.2	1.13	23	-50
19	216.76+26.13+100	08:31:45	08:28:54	5.7	64	2.33	0.84	28	100
20	218.47+25.07+104	08:30:43	06:37:48	6.1	61	2.53	0.79	28	104
21	218.81+15.33+089	07:56:36	01:52:08	7.7	91	4.79	1.1	26	89
22	239.80+69.44+043	11:35:06	16:35:54	5.5	63	1.29	0.47	30	43
23	291.07+62.01+024	12:29:17	-00:20:50	7.4	87	5.2	1.28	30	24
24	^V 299.01+68.15+269	12:45:35	05:19:27	6.1	50	1.79	0.7	20	269
25	307.78+71.61+131	12:57:37	08:47:58	7.6	112	6.36	1.41	26	131

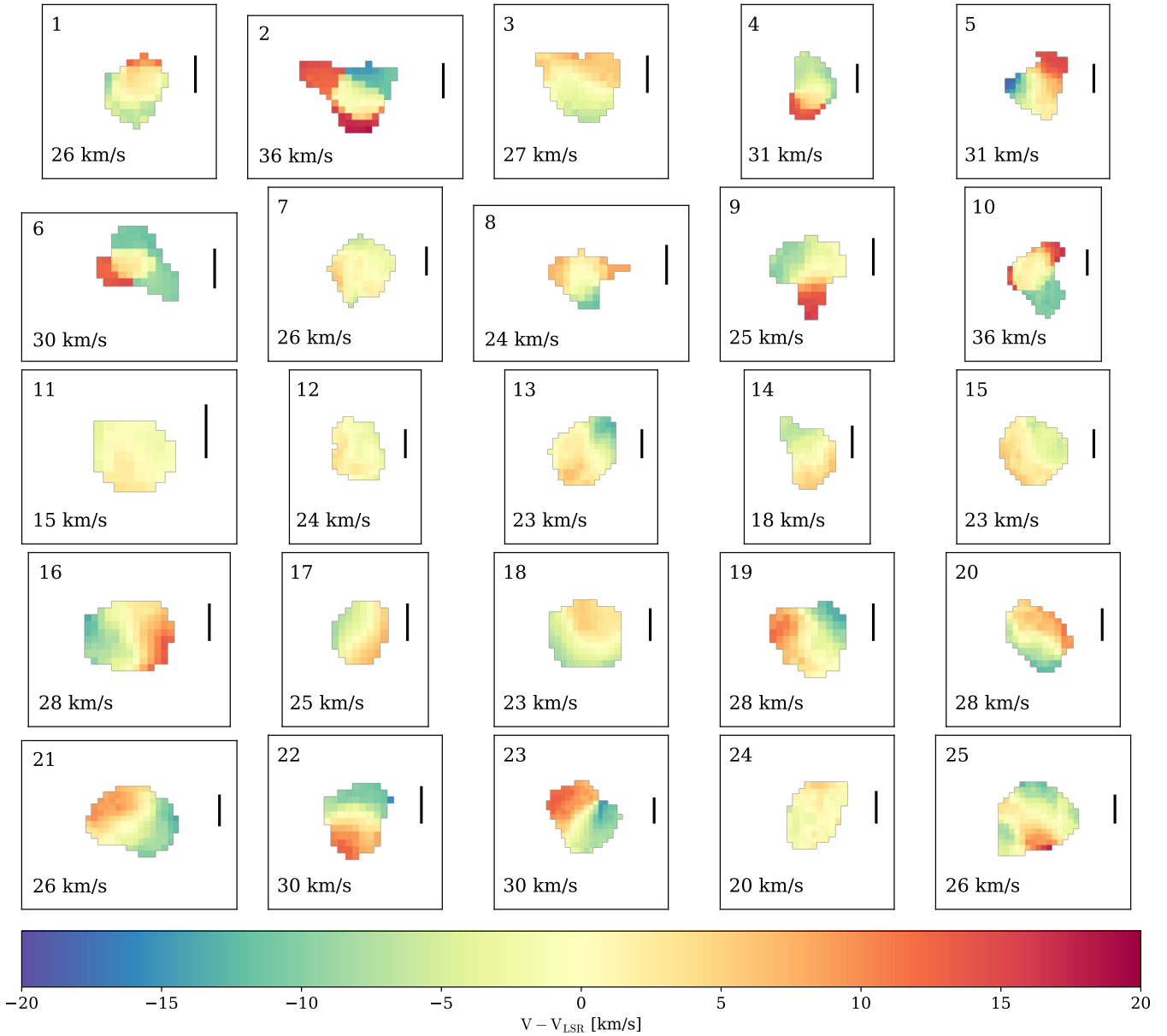


Figure 10. HI velocity maps of the sources in Table 5 in (R.A., decl.) coordinates. Red and blue colors correspond to velocities greater than and less than the systemic velocity, respectively. The numbers in the top left corners match with the entries in the first column of Table 5. The quantities in the bottom left corners are the corresponding velocity widths (w_{50}). The vertical black lines are each 5 arcmin long.